NANO LETTERS

Letter

pubs.acs.org/NanoLett

Functionalized Nanocellulose-Integrated Heterolayered Nanomats toward Smart Battery Separators

Jung-Hwan Kim,[†] Minsu Gu,[†] Do Hyun Lee,[†] Jeong-Hoon Kim,[†] Yeon-Su Oh,[†] Sa Hoon Min,[*,†] Byeong-Su Kim,[*,†,‡] and Sang-Young Lee[*,†]

[†]Department of Energy Engineering, School of Energy and Chemical Engineering and [‡]Department of Chemistry, School of Natural Science, Ulsan National Institute of Science and Technology (UNIST), Ulsan 44919, Republic of Korea

Supporting Information

ABSTRACT: Alternative materials obtained from natural resources have recently garnered considerable attention as an innovative solution to bring unprecedented advances in various energy storage systems. Here, we present a new class of heterolayered nanomat-based hierarchical/asymmetric porous membrane with synergistically coupled chemical activity as a nanocellulose-mediated green material strategy to develop smart battery separator membranes far beyond their current state-of-the-art counterparts. This membrane consists of a terpyridine (TPY)-functionalized cellulose nanofibril (CNF) nanoporous thin mat as the top layer and an electrospun polyvinylpyrrolidone (PVP)/polyacrylonitrile (PAN) macroporous thick mat as the support layer. The hierarchical/asymmetric porous structure of the heterolayered nanomat is rationally designed with consideration of the trade-off between leakage current and ion transport rate. The TPY (to chelate Mn^{2+} ions) and PVP (to capture hydrofluoric acid)-mediated chemical functionalities bring a synergistic coupling in suppressing Mn^{2+}-induced adverse effects, eventually enabling a substantial improvement in the high-temperature cycling performance of cells.

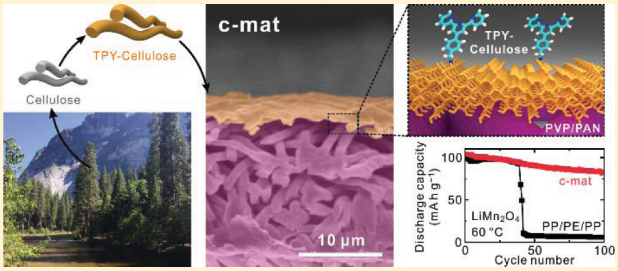

KEYWORDS: *Separator membranes, heterolayered nanomat, functionalized nanocellulose, metal-ion chelation, molecular simulation*

The rapidly approaching smart energy era, which will enjoy the widespread popularity of electric vehicles (EVs), grid-scale energy storage systems (ESSs), and flexible/wearable electronics, is strongly pushing us to develop advanced rechargeable batteries with reliable electrochemical performance.[1−3] As an innovative solution to address this challenging issue and also to fuel the sustainable growth of battery technologies, natural-resource-based alternative materials beyond the current state-of-the-art synthetic products have recently drawn substantial attention. Among the various eco-friendly materials reported to date, cellulose has been highlighted as a promising building block because of its natural abundance, low cost, physicochemical robustness, biocompatibility, lightweight, and recyclability.[4,5] Enormous efforts have been undertaken to use cellulose as an alternative natural material for a wide variety of rechargeable power sources such as lithium-ion and sodium-ion batteries and supercapacitors, with a focus on potential applications in electrode binders, mechanical buffers of metallic anodes, porous current collectors, and separator membranes.[6−9]

In the relentless pursuit of next-generation high-performance/high-safety batteries, a great deal of research interest should be devoted to the separator membranes as well as the electrodes and electrolytes. Internal short-circuit failure occurring between the electrodes, which is considered a primary cause of cell fires or explosions, can be prevented by separator membranes.[10−12] Meanwhile, as an essential prerequisite for activating the electrochemical reaction in batteries, ions should reach electrodes via the electrolyte-filled porous channels of the separator membrane. Given such an important function of separator membranes in the ion transport between electrodes, introducing novel chemical functionalities to separator membranes is expected to bring unprecedented benefits to battery performance. For example, unwanted byproducts in electrolytes, such as manganese ions (Mn^{2+}) dissolved from lithium manganese oxide electrode materials[13,14] and hydrofluoric acid (HF) generated by side reactions between residual water and lithium salts,[15] are known to result in serious capacity loss during charge/discharge cycling. These byproducts can be captured by separator membranes bearing suitable chemical functionality prior to reaching the electrodes. Unfortunately, very few studies have been performed to develop functionalized separator membranes, including the partial modification of polyolefin microporous membranes[16,17] and electrospun nonwovens.[18] In particular, the theoretical-understanding-based design and synthesis of chemically active groups in functional separator membranes, along with concurrent endeavors to promote ion transport kinetics, have not been reported.

Received: May 21, 2016
Revised: July 1, 2016
Published: July 6, 2016

DOI: 10.1021/acs.nanolett.6b02069
Nano Lett. 2016, 16, 5533−5541

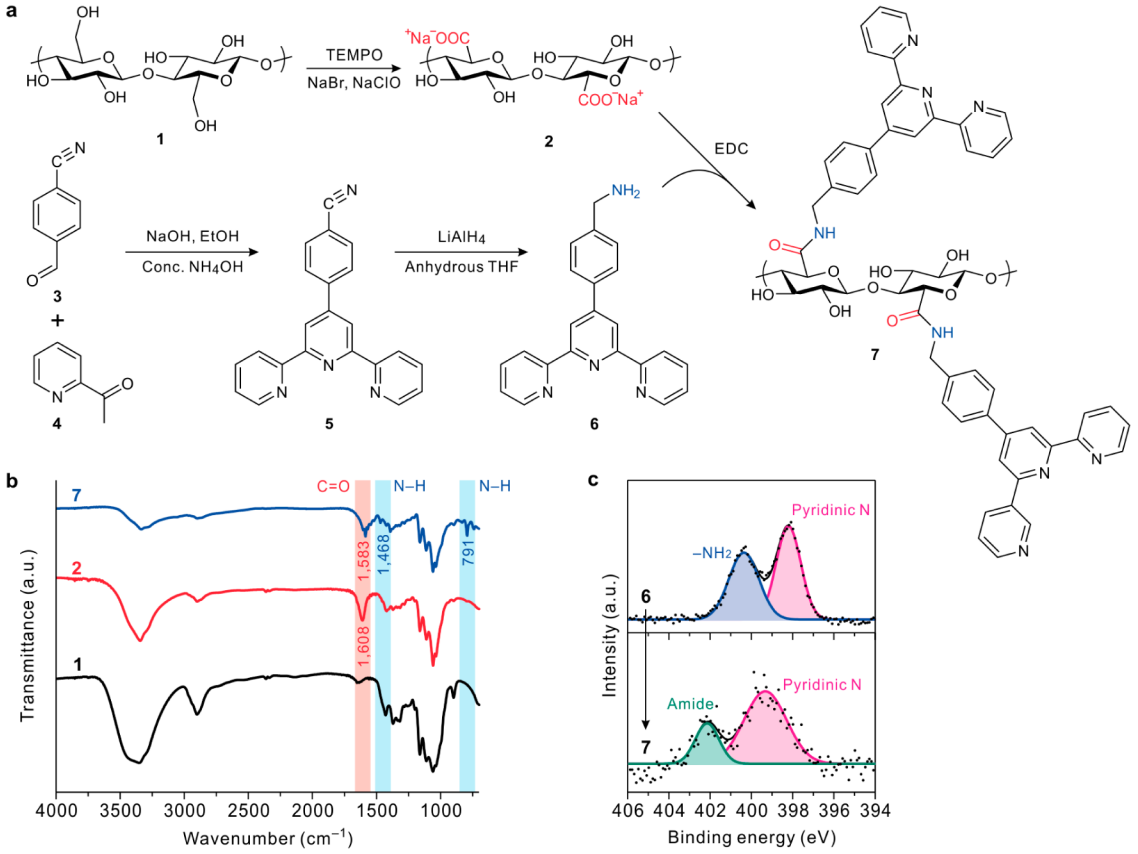

Figure 1. Synthesis of TPY-functionalized cellulose nanofibrils (CNFs). (a) Illustration of a TPY-functionalized CNF. (b) FT-IR spectra of CNF **1**, oxidized CNF **2**, and TPY-functionalized CNF **7**. (c) N 1s XPS spectra of amine-containing TPY **6** and TPY-functionalized CNF **7**.

Herein, intrigued by the facile functionalization of nanocellulose via its rich hydroxyl moieties, we propose a green material strategy for the development of next-generation separator membranes that can address the aforementioned long-standing challenges (i.e., internal short-circuit safety failure, ion transport kinetics, and chemical functionality). Specifically, we present a new class of heterolayered-nanomat-based hierarchical/asymmetric porous membranes with synergistically coupled chemical activity (referred to as the c-mat separator). The c-mat separator is composed of a terpyridine (TPY)-functionalized cellulose nanofibril (TPY-CNF) thin nanoporous mat as the top layer and an electrospun polyvinylpyrrolidone (PVP)/polyacrylonitrile (PAN) thick macroporous mat as the support layer. The TPY-CNF top layer is seamlessly integrated with the PVP/PAN support layer by a vacuum-assisted infiltration process. The TPY molecules, because of their electron-rich nitrogen groups in an array of π-conjugated geometries, readily coordinate with metals to form bis(terpyridine)/metal complexes $[M(TPY)_2]$.[19,20] In this study, Mn^{2+} ions dissolved from $LiMn_2O_4$ (LMO) are chosen as model metal ions dissolved in liquid electrolytes. Notably, the Mn^{2+}-chelating capability of TPY in TPY-CNF is theoretically investigated using density functional theory (DFT) calculations and molecular dynamics (MD) simulations. The TPY-CNF, in conjunction with the PVP acting as a HF scavenger, provides synergistic coupling in suppressing Mn^{2+}-induced adverse effects. In addition to this unusual chemical functionality, another salient feature of the c-mat separator is the one-dimensional (1D) fiber-based heterolayered nanomat architecture, which enables the construction of a hierarchical/asymmetric porous structure. In the thin top layer, nanoscale pores are formed between densely piled TPY-CNFs, thereby preventing leakage current between the electrodes. The macroporous electrospun PVP/PAN mat allows fast and facile ion transport through its highly developed, micrometer-sized porous channels that function like ionic highways. Benefiting from the aforementioned structural/chemical uniqueness, the c-mat separator is anticipated to provide substantial improvements in battery performance far beyond that achievable with conventional separator technologies.

To produce TPY-functionalized CNFs (TPY-CNFs), we rationally designed the synthetic reaction steps as follows (Figure 1a). Pristine CNFs were obtained through the repeated high-pressure mechanical disintegration of wood pulp.[21,22] The surface modification of CNFs was conducted using TEMPO-mediated oxidation to generate carboxylic acid/carboxylate groups that act as reactive branching sites. Because of the presence of the more hydrophilic carboxylate moiety, the solubility of the oxidized CNFs was enhanced in the aqueous suspension, yielding a lower viscosity (3.00 ± 1.79 cP) compared to that of the pristine CNF suspension (8.46 ± 0.37 cP). Meanwhile, amine-containing TPY molecules were synthesized and confirmed by ^{1}H NMR and mass spectrometry (Supporting Information, Figure S1). As-synthesized TPY was then conjugated with carboxylate groups on the oxidized CNFs in the presence of *N*-ethyl-*N*′-(3-(dimethylamino)propyl) carbodiimide methiodide (EDC), eventually leading to the TPY-CNFs.

The functional groups of the synthesized TPY-CNFs were identified through analysis of the corresponding FT-IR spectra

DOI: 10.1021/acs.nanolett.6b02069
Nano Lett. 2016, 16, 5533−5541

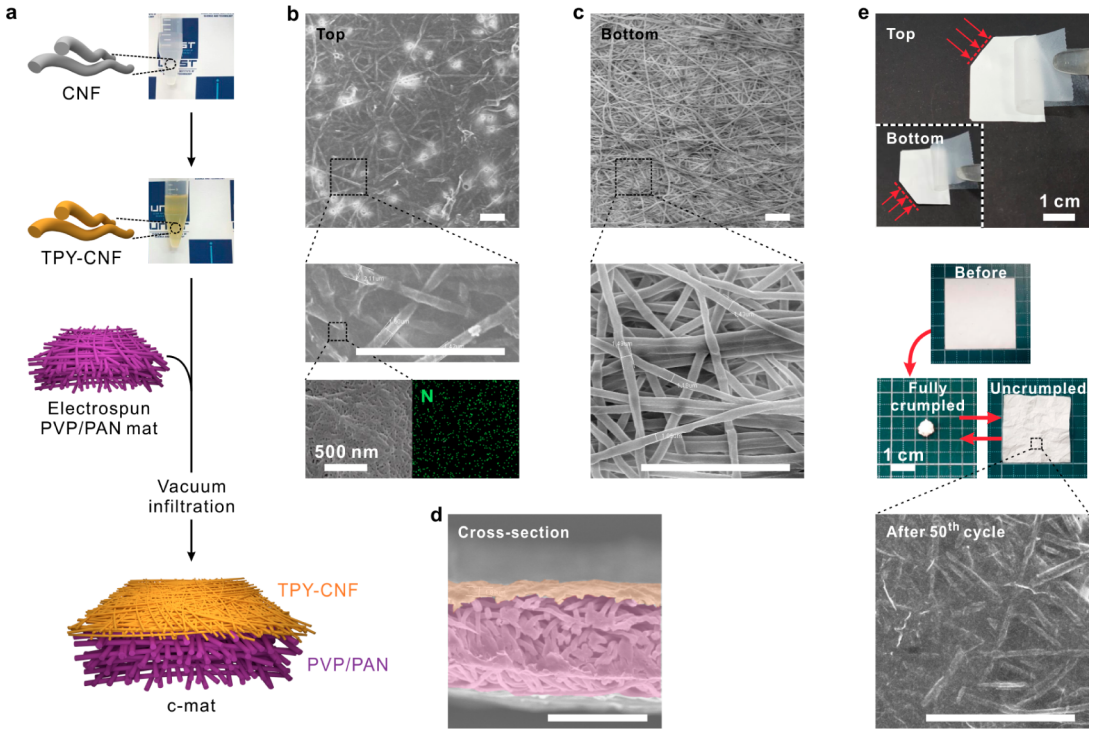

Figure 2. Fabrication and structural/physical characterizations of the c-mat separator. (a) Schematic depicting the overall fabrication procedure of the c-mat separator. SEM images of the (b) top, (c) bottom sides, and (d) cross-section of the asymmetric c-mat separator and an elemental mapping image of nitrogen. (e) A tape test using commercial Scotch tape, a crumpling test of the c-mat, and an SEM image after the 50th cycle. The scale bar of each SEM images is 20 μm.

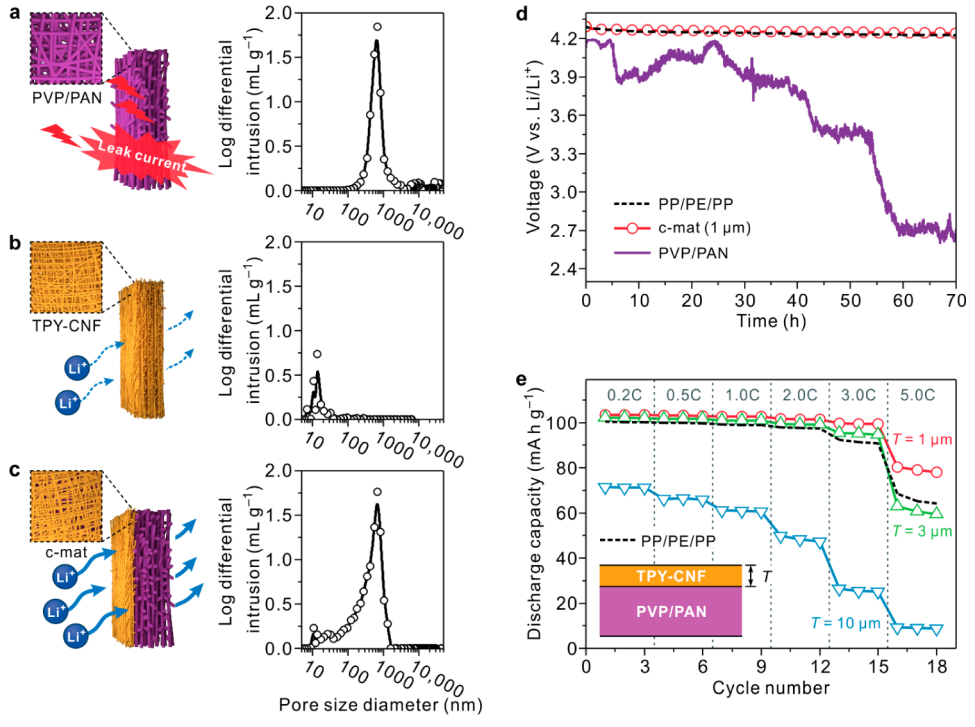

Figure 3. Comparison of the separators. Schematic and pore size distribution of the (a) PVP/PAN electrospun mat, (b) TPY-CNF, and (c) TPY-CNF on PVP/PAN (c-mat). (d) OCV profiles of the cells (LMO cathode/Li metal anode), where the cells were charged to 4.3 V at a constant current density of 0.2 C and their voltage drop was measured as a function of the elapsed time. (e) Discharge rate performance as a function of the thickness of the TPY-CNF layer.

(Figure 1b). For both the oxidized CNFs and the TPY-CNFs, the introduction of carboxylate groups caused the appearance of the C═O stretching vibration peak at 1610 cm^{-1}, which was absent in the spectrum of the pristine CNFs. In the spectrum of the TPY-CNFs, new peaks were observed at 1468 and 791 cm^{-1}, which were attributed to N−H bending and rocking of

DOI: 10.1021/acs.nanolett.6b02069
Nano Lett. 2016, 16, 5533−5541

amide, respectively, indicating the successful amide coupling by EDC chemistry. The TPY molecule bonded to the CNFs was further verified by analyzing the XPS spectra (Figure 1c). The characteristic N 1s peaks of the TPY-CNFs were observed at 402.1 (amide) and 399.3 eV (pyridinic-N); these peaks were shifted upward from those of the bare TPY molecules at 400.4 (amine) and 398.2 eV (pyridinic-N).

The c-mat separator was fabricated using a vacuum-assisted infiltration technique analogous to the traditional paper-making process.[23−25] The as-obtained TPY-CNF suspension was poured onto an electrospun PVP/PAN mat positioned inside a porcelain Büchner funnel. The uniform dispersion of the nanometer-scale TPY-CNF suspension is shown in the inset of Figure 2a. After the vacuum infiltration followed by solvent removal, a self-standing c-mat separator was successfully produced. A schematic depicting the overall fabrication procedure of the c-mat separator is provided in Figure 2a.

The structural uniqueness of the c-mat separator was characterized with a particular focus on its hierarchical/asymmetric porous morphology. A scanning electron microscopy (SEM) image of the c-mat separator shows that the 1D nanofibers (i.e., the TPY-CNFs) are densely packed and uniformly distributed over a wide area of the TPY-CNF mat, generating a number of nanoscale pores formed between the compactly piled TPY-CNFs (Figure 2b). Meanwhile, an EDS image reveals the presence of TPY molecules (their nitrogen atoms are represented in green) chemically linked to the CNFs. The opposite side of the c-mat separator was the electrospun PVP/PAN mat serving as a support layer (Figure 2c). Compared with the TPY-CNFs, the electrospun PVP/PAN fibers have a larger micron-sized diameter, thus yielding a highly interconnected macroporous structure in the resultant PVP/PAN support layer. A cross-sectional SEM image shows that the thin TPY-CNF mat (top layer) was integrated with the thick PVP/PAN mat (support layer) and that a hierarchical/asymmetric porous structure developed in the through-thickness direction (Figure 2d).

To check the structural/dimensional robustness of the c-mat separator, tape tests were conducted. No appreciable amount of TPY-CNFs or PVP/PAN fibers was detached from the c-mat separator (Figure 2e). Additionally, upon repeated crumpling/uncrumpling cycles, the c-mat separator maintained its dimensional stability without physically disintegrating into individual fibers (Figure 2e).

We note again that a morphological feature of the c-mat separator is the heterolayered nanomat-enabled hierarchical/asymmetric porous structure [i.e., the combination of the nanoporous structure (the TPY-CNF top layer) and the macroporous one (the PVP/PAN support layer)]. To elucidate the advantageous effect of this structural uniqueness on the electrochemical performance of cells, a PVP/PAN mat and a TPY-CNF mat were fabricated as model separators and subsequently compared with the c-mat separator. The porous morphology and pore size distribution (PSD) of the separator samples examined herein are shown in Figure 3a−c. The PVP/PAN separator (Figure 3a) clearly exhibited large-sized macropores, and the average diameter was estimated from the PSD to be ∼1000 nm. In comparison, the nanoporous structure (average diameter ∼10 nm) formed from the densely packed TPY-CNFs was observed at the TPY-CNF separator (Figure 3b). Notably, the c-mat separator exhibited the hierarchical (nanoporous-macroporous)/asymmetric porous structure in the through-thickness direction (Figure 3c), which was further verified by the bimodal pore size distribution.

The drop in the open-circuit voltage (OCV) and the discharge C-rate capability of the cells assembled with the aforementioned separators were characterized; the results are discussed in terms of the separators' porous structures.[26] The OCV drop test (Figure 3d), which is known to be an indicator of self-discharge behavior in cells, showed that the cell containing the macroporous PVP/PAN separator failed to maintain its charge voltage over time, revealing that the micrometer-scale pore size of the PVP/PAN separator is too large to sufficiently prevent leakage current between the electrodes. By contrast, no appreciable drop in the OCV was observed at the c-mat separator, which appeared to be comparable to that of a commercial PP/PE/PP separator (Supporting Information, Figure S2). The OCV results demonstrate that the nanoporous TPY-CNF top layer in the c-mat separator plays a critical role in suppressing leakage current.

Despite the beneficial contribution of the TPY-CNF top layer, its nanoporous structure may limit the ionic flux through the layer, thus negatively affecting the electrochemical performance of cells. To address this concern, various c-mat separators with TPY-CNF top layers of various thicknesses were fabricated. Figure 3e shows the effect of the top layer thickness on the discharge capacity of cells assembled with c-mat separators, wherein half-cells (i.e., LMO cathode/separator/Li metal anode) were charged at a constant current density of 0.2 C and were discharged at various current densities (0.2−5.0 C) in the voltage range from 3.0 to 4.3 V. As the top layer thickness was increased from 1 to 10 μm, the discharge capacities tended to decrease, which became more pronounced at higher discharge current densities. Notably, a serious drop in discharge capacities was observed at a thickness of 10 μm. The detailed discharge profiles of the cells are provided in the Supporting Information, Figure S3. These results demonstrate that the TPY-CNF top layer, because of its relatively less-developed porous structure, acts as a resistive layer to ionic conduction; they also demonstrate that the excessively large thickness of the top layer causes cell polarization, eventually deteriorating the discharge capacities, particularly at high current densities. One noteworthy finding is that the c-mat separator with the TPY-CNF top layer (thickness = 1 μm) delivered higher discharge capacities than the PP/PE/PP separator over a wide range of current densities, demonstrating that finely tuning the thickness of the nanoporous TPY-CNF top layer, in association with the integrated macroporous PVP/PAN support layer (acting as an ionic highway), allows fast/facile ion transport while simultaneously preventing the leakage current between the electrodes. In other words, under the condition that leakage current of cells is strictly suppressed, the thinner top layer is beneficial for achieving the faster ion transport, eventually leading to the superior cell performance. Future works will be devoted to fine-tuning porous structure of the top and support layers by material/process control, which is expected to allow additional decrease in the thickness of the top layer. Schematics depicting the effects of the porous structure of the separators on the leakage current and on the ion transport between the electrodes are presented in Figure 3.

In addition to the aforementioned structural uniqueness, another salient feature of the c-mat separator is the chemical functionalities achieved by TPY-CNFs (in the top layer) and PVP (in the support layer). We theoretically investigated the

DOI: 10.1021/acs.nanolett.6b02069
Nano Lett. 2016, 16, 5533−5541

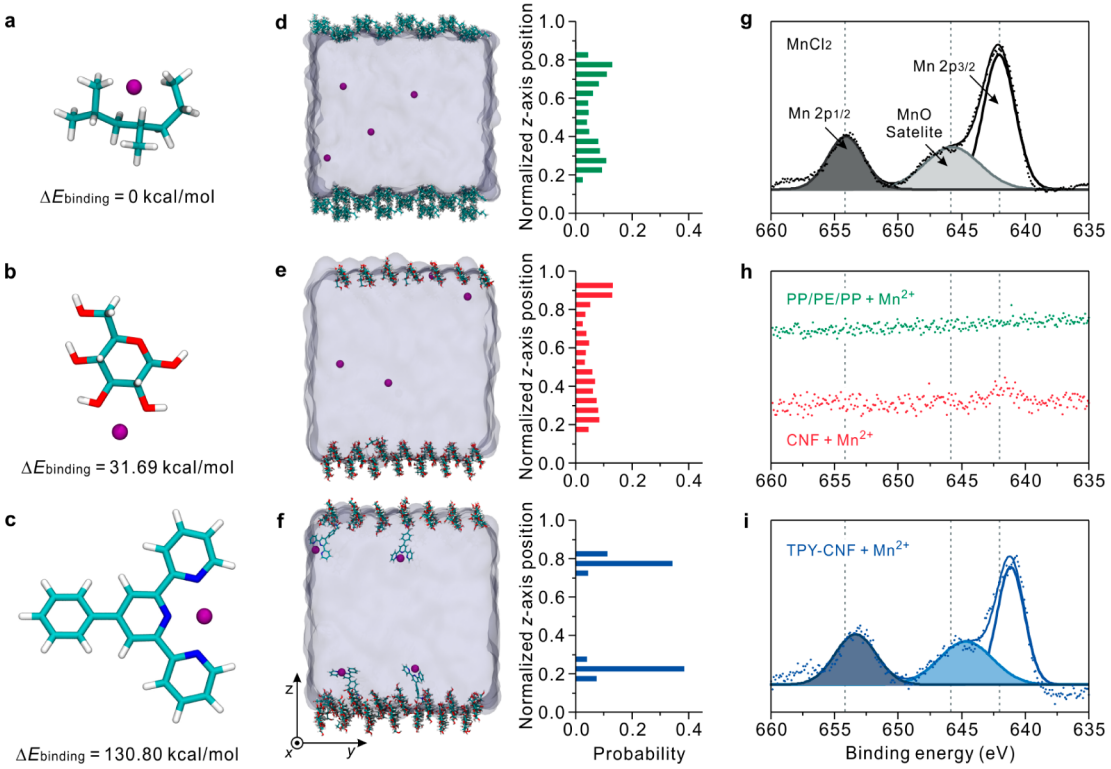

Figure 4. Mn^{2+} ion binding capability of TPY-CNF. B3LYP/6-31G(d,p)-optimized geometries of (a) $Mn^{2+}(PP_3)$, (b) Mn^{2+}(Glc), and (c) Mn^{2+}(TPY) complexes with the relative binding energies from DFT calculations at B3LYP/6-311+G(2d,2p) level, including BSSE corrections. Equilibrium morphologies after a 400 ns MD simulation at 333 K and normalized *z*-axis position probability of Mn^{2+} ions for the last 100 ns on the surface of (d) PP, (e) cellulose, and (f) TPY-cellulose. Violet beads represent the Mn^{2+} ions, and the ethylene carbonate solvent is shown as a transparent surface for clarity. Deconvoluted high-resolution Mn 2p XPS spectra of (g) $MnCl_2$, (h) PP/PE/PP, CNF, and (i) TPY-CNF with Mn^{2+} ions.

metal ion (here, Mn^{2+} ion) chelation of TPY-CNFs by performing DFT calculations. As a control, a plain PP separator was chosen. Considering the possible binding sites of Mn^{2+} ions, the PP, CNF, and TPY were simplified to trimers of PP (PP_3), α-D-glucose (Glc), and TPY molecules, respectively. The optimized geometries and binding energies of the Mn^{2+} complex were calculated at the B3LYP/6-311+G(2d,2p)//B3LYP/6-31G(d,p) level with BSSE corrections using the Gaussian 09 program.[27]

On the basis of the binding energy of the $Mn^{2+}(PP_3)$ complex, Figure 4a–c shows that Mn^{2+}(Glc) and Mn^{2+}(TPY) complexes have large differences in their binding energies, which are 31.69 kcal mol^{-1} and 130.80 kcal mol^{-1}, respectively. Whereas the Mn–H interaction is dominant in the $Mn^{2+}(PP_3)$ complex, the optimized geometry of the Mn^{2+}(Glc) complex indicates a relatively strong interaction between the Mn^{2+} ion and the lone-pair electrons in the hydroxyl oxygen atom. In particular, the high binding energy of the Mn^{2+}(TPY) complex results from the electrostatic interactions and charge transfer between the Mn^{2+} ion and the pyridine groups in TPY with the coordinated structure.

The binding stability of the Mn^{2+} ions on the model surfaces of PP, CNFs, and TPY-CNFs was also investigated using MD simulations. The calculations were performed using the AMBER 14 software;[28] the detailed procedure is described in the Supporting Information. The Mn^{2+} ions were initially positioned at each model surface on the basis of the geometries determined from the DFT calculations. In the isothermal-isobaric (NPT) simulations of 400 ns at 333 K, the *z*-axis position of the Mn^{2+} ions was tracked during the last 100 ns.

As shown in Figure 4d, the Mn^{2+} ions were located in the region of the ethylene carbonate (EC) solvent while being detached from the PP surface. The probability of the *z*-axis position shows that Mn^{2+} ions could move freely in the EC solvent, representing the absence of specific interactions between the Mn^{2+} ions and the PP surface. By contrast, the nanocellulose surface still held a Mn^{2+} ion by the hydroxyl groups of the glucose unit after 400 ns (Figure 4e). The high probability around the CNF surface demonstrates that Mn^{2+} ions have relatively strong interactions with the CNF surface compared with that of PP. As expected, the terpyridine groups in the TPY-CNFs maintained their coordination structure with the Mn^{2+} ions during the MD simulation (Figure 4f) because of the high interaction energy between them. As a result, the probability of the *z*-axis position of the Mn^{2+} ions is obviously concentrated at the surface of the TPY-CNFs.

On the basis of the aforementioned simulation results, the Mn^{2+} ion binding capability of the TPY-CNFs was experimentally verified. The TPY-CNFs, along with the PP/PE/PP separator and the pristine CNFs, were soaked in 1 M $MnCl_2$ solution, and the change in their XPS Mn 2p spectra was analyzed (Figure 4g–i). The TPY-CNFs showed the appearance of Mn 2p peaks, whereas no appreciable Mn 2p peaks were observed at the PP/PE/PP separator or the pristine CNFs. Furthermore, the deconvoluted peaks of the TPY-CNFs shifted downward from 654.1 (Mn $2P_{1/2}$), 645.8 (MnO satellite), and 642.1 eV (Mn $2P_{3/2}$) to 653.4, 644.7, and 641.1 eV, respectively, verifying metal–ligand coordination via the electron-donating of the TPY ligands. The aforementioned theoretical (by DFT calculations and MD simulations) and

DOI: 10.1021/acs.nanolett.6b02069
Nano Lett. 2016, 16, 5533–5541

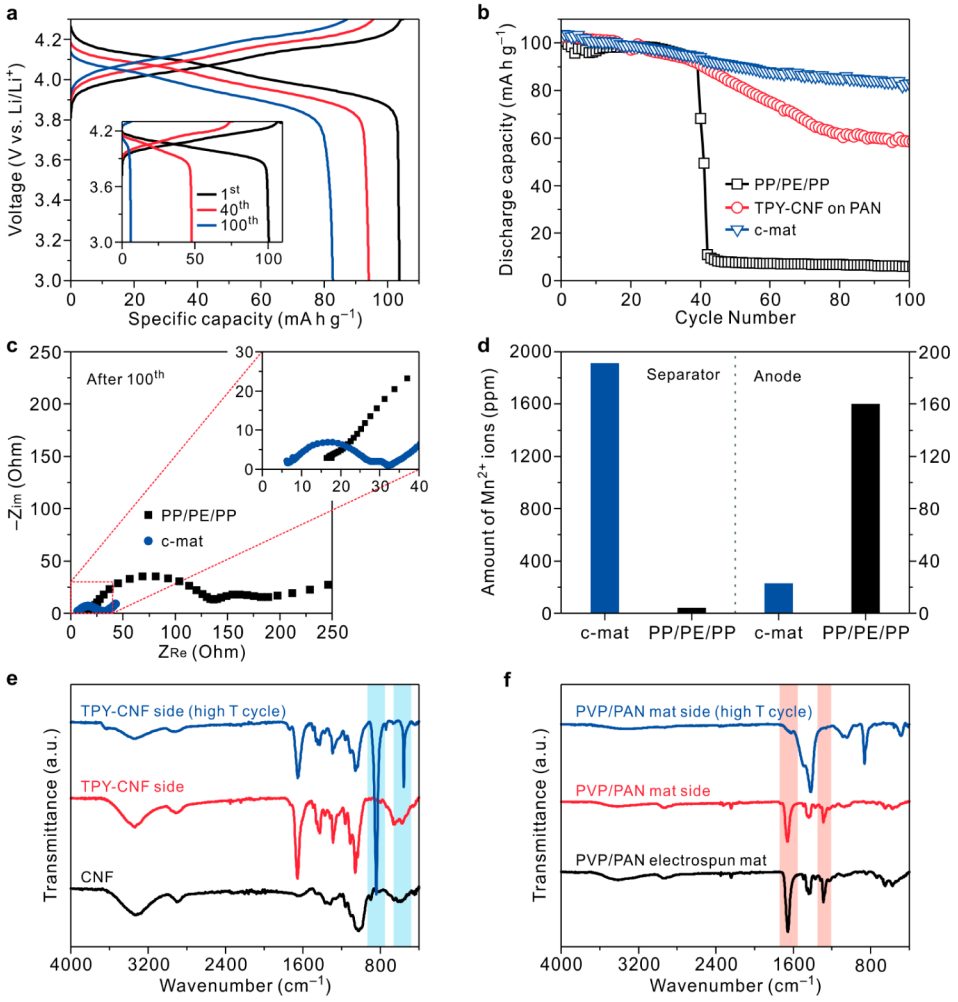

Figure 5. Cell performance of the c-mat and PP/PE/PP separators. (a) Charge/discharge profiles with cycling (100 cycles) at 60 °C. (b) High-temperature (60 °C) capacity retention as a function of cycle number. (c) AC impedance spectra after 100 cycles at 60 °C. (d) Amount of Mn^{2+} ions captured by separators and deposited on the Li metal anode (estimated from ICP-MS analysis). FT-IR spectra of the (e) TPY-CNF side and (f) PVP/PAN side of the c-mat separator after 100 cycles at 60 °C.

experimental (by XPS spectra) analyses together demonstrate the exceptional functionality of the TPY-CNF in Mn^{2+} chelation, which is therefore anticipated to play a viable role as a chemically active component of the c-mat battery separator.

The pyrrolidone rings of PVP, enabled by their Lewis basicity, are known to effectively scavenge HF dissolved in the electrolyte solution.[29] However, the bare PVP mat (without a PAN component) was chemically vulnerable to the electrolyte solution, resulting in the loss of its dimensional stability (Supporting Information, Figure S4a). This problem with PVP was resolved by exploiting a polymer blending strategy in which PAN was mixed with PVP. At the composition ratio of 50:50 (w/w), the resultant PVP/PAN mats maintained their dimensional integrity in the electrolyte solution (Supporting Information, S4b). As a supplementary experiment to identify the HF-scavenging capability, the PVP/PAN mat was soaked for 24 h in an electrolyte solution (1 M $LiPF_6$ in EC/diethyl carbonate (DEC) = 1/1 (v/v)) containing 100 ppm of HF, and the change in its XPS spectra was monitored (Supporting Information, Figure S5). The characteristic N 1s peak assigned to the nitrogen of pyrrolidone shifted upward, and a new peak appeared at approximately 400.5 eV, indicating the possible formation of new N−H bonds between pyrrolidone and HF. In comparison, no appreciable change in the N 1s peak was observed for the electrolyte-soaked PAN mat. These results demonstrate the important role of PVP in chemically scavenging HF.

Prior to exploring the electrochemical performance of the c-mat separator for use in lithium-ion batteries, we characterized its basic membrane properties. The c-mat separator exhibited a higher ion conductivity than the PP/PE/PP separator, which was further confirmed by comparison of their air permeability (represented by the Gurley value) and their porosity (Supporting Information, Table S1). These results demonstrate the c-mat separator's superior ionic flux stemming from its unusual hierarchical/asymmetric porous structure. The linear sweep voltammetry (LSV) results showed that the c-mat separator was electrochemically stable to 4.5 V (vs Li/Li^+), comparable to the stability of the PP/PE/PP separator (Supporting Information, Figure S6a). The c-mat separator, as a consequence of its polar components and well-developed porous structure, exhibited a higher electrolyte-immersion height (i.e., better electrolyte wettability) than the PP/PE/PP separator (Supporting Information, Figure S6b). This superior wettability was further underscored by examining charge/

DOI: 10.1021/acs.nanolett.6b02069
Nano Lett. 2016, 16, 5533−5541

discharge profiles of cells containing extremely polar electrolyte (here, 1 M $LiPF_6$ in EC/PC = 1:1 (v/v)) was chosen as a representative electrolyte). The cell (LMO cathode/separator/$Li_4Ti_5O_{12}$ anode) assembled with the c-mat separator showed the normal charge/discharge behavior and the stable cycling performance, whereas the cell with the PP/PE/PP separator was unable to be electrochemically activated (Supporting Information, Figure S6c). No thermal shrinkage was observed in the c-mat separator upon exposure to 150 °C/0.5 h (Supporting Information, Figure S6d), demonstrating its excellent thermal tolerance compared to that of the PP/PE/PP separator.

To investigate the effects of the c-mat separator on cell performance, a pouch-type cell (width × length = 30 × 40 mm^2) was assembled with a LMO cathode and a Li metal anode, in which the TPY-CNF top layer was in contact with the LMO cathode while the PVP/PAN support layer faced the Li metal anode. The c-mat separator, because of its faster ion transport rate (Supporting Information, Table S1), exhibited a higher discharge capacity than the PP/PE/PP separator over a wide range of discharge current densities (ranging from 0.2 to 5.0 C), which became more noticeable at higher discharge current densities (Supporting Information, Figure S7a). To further highlight the advantageous effect of the c-mat separator, electrochemical performance of a full cell (comprising $LiCoO_2$ (LCO) cathode and natural graphite anode) was examined. The full cell was assembled by sandwiching a separator between LCO cathode (LCO/carbon black/PVdF binder = 95:2:3 (w/w/w)) and natural graphite anode (natural graphite/carbon black/PVdF binder = 90:2:8 (w/w/w)) and then activated by filling the liquid electrolyte. The cells were charged at a constant current density of 0.2 C and were discharged at various current densities (0.2−5.0 C) under a voltage range of 3.0−4.2 V. Similar to the result (Supporting Information, Figure S7a) obtained with the half cells, the c-mat separator showed the better discharge C-rate capability than the PP/PE/PP separator (Supporting Information, Figure S7b).

The cycling performance of cells was examined, and the cells were cycled between 3.0 and 4.3 V at a charge/discharge current density of 1.0C/1.0C. At room temperature, the c-mat separator exhibited a cycling performance superior to that of the PP/PE/PP separator (Supporting Information, Figure S7c). This advantageous effect of the c-mat separator was more pronounced during the high-temperature (60 °C) cycling test. The cell incorporating the c-mat separator delivered stable charge/discharge profiles for 100 cycles (Figure 5a). By comparison, the cell with the PP/PE/PP separator showed a sharp decay in the capacity and large cell polarization after 100 cycles (see the inset of Figure 5a), which were mainly attributed to undesirable Mn^{2+} dissolution from the LMO active materials at high temperatures, as previously reported.[18,30,31] The capacity retention after 100 cycles was estimated to be approximately 80% for the c-mat separator compared to 5% for the PP/PE/PP separator (Figure 5b). This superior capacity retention of the c-mat separator was confirmed through analysis of the variation in the AC impedance spectra of cells before/after 100 cycles (Figure 5c and Supporting Information, Figure S8a). The c-mat separator was better able to suppress the growth of cell impedance after 100 cycles (Z_{Re} (100th cycle) − Z_{Re} (1st cycle) = $\Delta Z_{Re} \approx 17\ \Omega$) compared with the PE separator ($\Delta Z_{Re} \approx 175\ \Omega$). A proper equivalent circuit model was also presented to further analyze the cell impedance spectra in terms of the bulk resistance (R_b), SEI resistance (R_{sf}), and charge transfer resistance (R_{ct}) (Supporting Information, Figure S8b).[32] Notably, the c-mat separator exhibited a more substantial decrease in charge transfer resistance compared to that of the PP/PE/PP separator, verifying the Mn^{2+} chelation-enabled stabilization of the electrode/electrolyte interface. In addition, the long-term structural stability of the c-mat separator after the cycling test (100 cycles) was examined. Neither morphological disruptions nor structural defects were observed at the TPY-CNF top layer and also the PVP/PAN support layer of the c-mat separator (Supporting Information, Figure S9).

Meanwhile, a supplementary experiment was conducted to investigate the effect of separator position on cell performance. In one cell (named as cell I), the TPY-CNF top layer was in contact with the LMO cathode. The other cell (cell II) had the opposite configuration (i.e., the TPY-CNF top layer was positioned toward the Li metal anode). Intriguingly, cell I showed the superior cycling performance compared to cell II (Supporting Information, Figure S10). This result demonstrates that the Mn^{2+} chelation enabled by the TPY-CNF top layer is more effective when the top layer is in close contact with the LMO cathode.

To highlight the unusual chemical functionalities (i.e., Mn^{2+} chelation by TPY-CNF and HF capture by PVP) of the c-mat separator, we fabricated a control separator comprising a TPY-CNF top layer and an electrospun PAN support layer (without PVP) and compared its cycling performance with that of the c-mat separator (Figure 5b). The control separator showed significant improvement in retaining the capacity during cycling compared to the PP/PE/PP separator, indicating that TPY is effective in chelating the Mn^{2+} ions dissolved from the LMO active materials. A notable finding is that the c-mat separator exhibited cycling performance superior to that of the control separator. This result indicates that the introduction of PVP into the support layer also contributed to the improvement in the high-temperature cycling performance, underlying the exceptional synergistic coupling of TPY and PVP as chemically active components.

The excellent high-temperature cycling performance of the c-mat separator was examined in detail, with particular attention to its Mn^{2+}-chelating and HF-scavenging capability. After the cycling test (100 cycles) at 60 °C, the cells were disassembled, and their major components, including the lithium metal anodes and separators, were characterized. The amount of Mn^{2+} ions captured by the separators was quantitatively analyzed by ICP-MS technique. Figure 5d shows that the c-mat separator more effectively chelated Mn^{2+} ions than the PP/PE/PP separator (amount of captured Mn^{2+} ions = 1915 ppm for the c-mat separator vs. 42 ppm for the PP/PE/PP separator). Furthermore, the deposition of metallic Mn on lithium metal anodes was remarkably alleviated by the c-mat separator (amount of deposited metallic Mn = 23 ppm for the c-mat separator vs 160 ppm for the PP/PE/PP separator). In addition to the ICP-MS measurement, the chemical changes of the separator surface were investigated through analysis of the FT-IR spectra (Figure 5e,f). The characteristic peaks assigned to the Mn−N stretching vibrations[33,34] (553 and 851 cm^{-1} for TPY-CNF side, Figure 5e) newly appeared in the spectrum of the c-mat separator. Moreover, the peaks corresponding to C═O/C−N groups[35] (1661 cm^{-1}/1285 cm^{-1}, respectively, for the PVP/PAN side, Figure 5f) decreased in intensity after the cycling test. The aforementioned ICP-MS and FT-IR results confirm that the TPY (for Mn^{2+} chelation) and the PVP (for

DOI: 10.1021/acs.nanolett.6b02069
Nano Lett. 2016, 16, 5533−5541

HF capture) of the c-mat separator exhibit synergistically coupled chemical functionalities that improve its high-temperature cycling performance.

In summary, we demonstrated the heterolayered nanomat-based hierarchical/asymmetric porous membranes with synergistically coupled chemical functionalities (referred to as c-mat separators) as a nanocellulose-mediated green material approach to develop smart battery separators beyond the current state-of-the-art counterparts. The c-mat separator consisted of a thin nanoporous TPY-CNF mat as the top layer and a thick macroporous electrospun PVP/PAN mat as the support layer. The unusual porous structure of the c-mat separator was rationally designed considering the trade-off between leakage current and ion transport rate, eventually contributing to the higher discharge rate capability without suffering a drop in the OCV. The TPY molecules were conjugated with TEMPO-oxidized CNFs mediated by EDC chemistry. Notably, their Mn^{2+}-chelating capability was also theoretically supported using DFT calculations/MD simulations; the results of these calculations/simulations were consistent with the experimental results. Meanwhile, the PVP in the PVP/PAN support layer served as an HF scavenger. The TPY and PVP, as the chemically active components of the c-mat separator, exhibited synergistic coupling in mitigating the Mn^{2+}-induced adverse effects, thereby enabling a remarkable improvement in the high-temperature (60 °C) cycling performance (capacity retention ~80% after 100 cycles) far beyond that attainable with conventional membrane technologies (5% for commercial PP/PE/PP separator). We envision that the c-mat separator, benefiting from its structural uniqueness and chemical functionalities, will open a new path for the development of high-performance smart separator membranes for potential use in next-generation power sources and in permselective membrane filtration systems for high mass flux/removal of heavy-metal ions.

■ ASSOCIATED CONTENT

Supporting Information

The Supporting Information is available free of charge on the ACS Publications website at DOI: 10.1021/acs.nanolett.6b02069.

Details of methods and supplementary results. Experimental procedures, calculation and simulation details, additional structural/membrane properties of c-mat separators, and electrochemical performance of cells (PDF)

■ AUTHOR INFORMATION

Corresponding Authors

*E-mail: (S.H.M.) minshu21@unist.ac.kr.
*E-mail: (B.-S.K.) bskim19@unist.ac.kr.
*E-mail: (S.-Y.L.) syleek@unist.ac.kr.

Author Contributions

J.-H.K. and M.G. contributed equally. J.-H.K., M.G., S.H.M., B.-S.K., and S.-Y.L. participated in conceiving and designing the project. J.-H.K. and M.G. contributed to preparing the samples and conducted data analysis. D.H.L. assisted with the synthesis of TPY-functionalized cellulose. J.-H.K. and Y.-S.O. assisted the electrochemical analysis. S.H.M. designed and conducted DFT calculations and MD simulations. B.-S.K. and S.-Y.L. coordinated and supervised the overall project. All authors discussed the results and participated in manuscript preparation.

Notes

The authors declare no competing financial interest.

■ ACKNOWLEDGMENTS

This work was supported by the Basic Science Research Program through the National Research Foundation of Korea (NRF) funded by the Ministry of Science, ICT and future Planning (2014R1A2A1A11052829, 2015R1A2A1A01003474, 2015R1A2A2A04003160). This work was also supported by the Industrial Technology Innovation Program 2015(10050568), funded by the Ministry of Trade, Industry & Energy (MOTIE). M.G. acknowledges financial support from the Global Ph.D. Fellowship funded by the NRF (NRF-2013H1A2A1033278).

■ REFERENCES

(1) Armand, M.; Tarascon, J.-M. *Nature* **2008**, *451*, 652−657.
(2) Tollefson, J. *Nature* **2008**, *456*, 436−440.
(3) Dunn, B.; Kamath, H.; Tarascon, J.-M. *Science* **2011**, *334*, 928−935.
(4) Habibi, Y.; Lucia, L. A.; Rojas, O. J. *Chem. Rev.* **2010**, *110*, 3479−3500.
(5) Moon, R. J.; Martini, A.; Nairn, J.; Simonsen, J.; Youngblood, J. *Chem. Soc. Rev.* **2011**, *40*, 3941−3994.
(6) Leijonmarck, S.; Cornell, A.; Lindbergh, G.; Wågberg, L. *Nano Energy* **2013**, *2*, 794−800.
(7) Zhu, H.; Jia, Z.; Chen, Y.; Weadock, N.; Wan, J.; Vaaland, O.; Han, X.; Li, T.; Hu, L. *Nano Lett.* **2013**, *13*, 3093−3100.
(8) Hu, L.; Pasta, M.; Mantia, F. L.; Cui, L.; Jeong, S.; Deshazer, H. D.; Choi, J. W.; Han, S. M.; Cui, Y. *Nano Lett.* **2010**, *10*, 708−714.
(9) Chun, S.-J.; Choi, E.-S.; Lee, E.-H.; Kim, J. H.; Lee, S.-Y.; Lee, S.-Y. *J. Mater. Chem.* **2012**, *22*, 16618−16626.
(10) Arora, P.; Zhang, Z. *Chem. Rev.* **2004**, *104*, 4419−4462.
(11) Zhang, S. S. *J. Power Sources* **2007**, *164*, 351−364.
(12) Lee, H.; Yanilmaz, M.; Toprakci, O.; Fu, K.; Zhang, X. *Energy Environ. Sci.* **2014**, *7*, 3857−3886.
(13) Whittingham, M. S. *Chem. Rev.* **2004**, *104*, 4271−4301.
(14) Zhan, C.; Lu, J.; Kropf, A. J.; Wu, T.; Jansen, A. N.; Sun, Y.-K.; Qiu, X.; Amine, K. *Nat. Commun.* **2013**, *4*, 2437.
(15) Xu, K. *Chem. Rev.* **2004**, *104*, 4303−4417.
(16) Yim, T.; Ha, H.-J.; Park, M.-S.; Kim, K. J.; Yu, J.-S.; Kim, Y.-J. *RSC Adv.* **2013**, *3*, 25657−25661.
(17) Woo, S. H.; Lim, H.-W.; Jeon, S.; Travis, J. J.; George, S. M.; Lee, S.-H.; Jo, Y. N.; Song, J. H.; Jung, Y. S.; Hong, S. Y.; Choi, N.-S.; Lee, K. T. *J. Electrochem. Soc.* **2013**, *160*, A2234−A2243.
(18) Kim, J.-M.; Kim, C.; Yoo, S.; Kim, J.-H.; Kim, J.-H.; Lim, J.-M.; Park, S.; Lee, S.-Y. *J. Mater. Chem. A* **2015**, *3*, 10687−10692.
(19) Chen, H.; Tagore, R.; Das, S.; Incarvito, C.; Faller, J. W.; Crabtree, R. H.; Brudvig, G. W. *Inorg. Chem.* **2005**, *44*, 7661−7670.
(20) Sakamoto, R.; Wu, K.-H.; Matsuoka, R.; Maeda, H.; Nishihara, H. *Chem. Soc. Rev.* **2015**, *44*, 7698−7714.
(21) Chun, S.-J.; Lee, S.-Y.; Doh, G.-H.; Lee, S.; Kim, J. H. *J. Ind. Eng. Chem.* **2011**, *17*, 521−526.
(22) Nogi, M.; Iwamoto, S.; Nakagaito, A. N.; Yano, H. *Adv. Mater.* **2009**, *21*, 1595−1598.
(23) Leijonmarck, S.; Cornell, A.; Lindbergh, G.; Wågberg, L. *J. Mater. Chem. A* **2013**, *1*, 4671−4677.
(24) Choi, K.-H.; Cho, S.-J.; Chun, S.-J.; Yoo, J. T.; Lee, C. K.; Kim, W.; Wu, Q.; Park, S.-B.; Choi, D.-H.; Lee, S.-Y.; Lee, S.-Y. *Nano Lett.* **2014**, *14*, 5677−5686.
(25) Cho, S.-J.; Choi, K.-H.; Yoo, J.-T.; Kim, J.-H.; Lee, Y.-H.; Chun, S.-J.; Park, S.-B.; Choi, D.-H.; Wu, Q.; Lee, S.-Y.; Lee, S.-Y. *Adv. Funct. Mater.* **2015**, *25*, 6029−6040.
(26) Kim, J.-H.; Kim, J.-H.; Choi, K.-H.; Yu, H. K.; Kim, J. H.; Lee, J. S.; Lee, S.-Y. *Nano Lett.* **2014**, *14*, 4438−4448.

DOI: 10.1021/acs.nanolett.6b02069
Nano Lett. 2016, 16, 5533−5541

(27) Frisch, M. J.; Trucks, G. W.; Schlegel, H. B.; Cheeseman, J. R.; Scalmani, G.; Barone, V.; Mennucci, B.; Petersson, G. A. *Gaussian 09, revision C. 01*; Gaussian Inc., 2010.
(28) Case, D. A.; Babin, V.; Berryman, J. T.; Betz, R. M.; Cai, Q.; Cerutti, D. S.; Cheatham, T. E., III; Darden, T. A.; Duke, R. E.; Gohlke, H. *AMBER 14*; University of California, 2014.
(29) Kim, J.-M.; Park, J.-H.; Lee, C. K.; Lee, S.-Y. *Sci. Rep.* **2014**, *4*, 4602.
(30) Cho, J.; Kim, T.-J.; Kim, Y. J.; Park, B. *Chem. Commun.* **2001**, 1074−1075.
(31) Lim, S.; Cho, J. *Chem. Commun.* **2008**, 4472−4474.
(32) Han, S. C.; Singh, S. P.; Hwang, Y.-H.; Bae, E. G.; Park, B. K.; Sohn, K.-S.; Pyo, M. *J. Electrochem. Soc.* **2012**, *159*, A1867−A1873.
(33) Akyüz, S. *J. Mol. Struct.* **1999**, *482*, 171−174.
(34) Aghatabay, N. M.; Neshat, A.; Karabiyik, T.; Somer, M.; Haciu, D.; Dülger, B. *Eur. J. Med. Chem.* **2007**, *42*, 205−213.
(35) Borodko, Y.; Habas, S. E.; Koebel, M.; Yang, P.; Frei, H.; Somorjai, G. A. *J. Phys. Chem. B* **2006**, *110*, 23052−23059.

DOI: 10.1021/acs.nanolett.6b02069
Nano Lett. 2016, 16, 5533−5541